1 *Mineral phases in metakaolin-portlandite pastes cured 15 years at 60ºC. New data for*
2 *scientific advancement*

3

4 *M. Frías[1,*], R. Vigil de la Villa[2], S. Martínez-Ramírez[3], R. García-Giménez[2], M.I.*
5 *Sánchez de Rojas[1]*

6 [1] Deparment of Materials, Eduardo Torroja Institute for Construction Science (IETcc-
7 CSIC), Madrid, 28033, Spain.

8 [2] Department of Geology and Geochemistry, Associated Unit CSIC-UAM
9 (Geomateriales), Sciences Faculty, UAM, Madrid, 28049, Spain

10 [3] Department of Nuclear, Vibrational and Disordered Media Spectroscopy, Institute for
11 the Structure of Matter (IEM-CSIC), Madrid, 28006, Spain

12 *Corresponding author M. Frías (e-mail: mfrias@ietcc.csic.es)

13 **Abstract**

14 One of the problems addressed by the scientific community in connection with cement

15 matrix hydration is the evolution of hydrated phases under certain, primarily

16 temperature-related, curing conditions. Such conditions are of utmost importance when

17 the cement generates metastable hydrated phases that develop into stable phases,

18 inducing substantial physical-mechanical changes in the matrix. One such instance

19 arises during the pozzolanic reaction between metakaolinite and calcium hydroxide at

20 60 °C when metastable hexagonal phases co-exist with cubic stable phases. Such

21 processes are well understood in the short and medium term (<5 years). Evolution at

22 longer curing times has not been studied, however. This paper describes the evolution of

23 the initial (stable and metastable) mineral phases in the metakaolinite / $Ca(OH)_2$

24 reaction toward a zeolite-like phase after 15 year curing at 60 °C. An understanding of

25 such mineralogical changes is scientifically significant, given their direct impact on the

26 engineering properties of cement-based matrices.

27 **Keywords:** Metakaolinite, pozzolanic reaction, metastable phases, temperature,
28 mineralogical evolution, zeolites.

29

1. INTRODUCTION

For decades, the inclusion of calcined alumino-silica pozzolans in cement matrices (Gbozee et al., 2018) has prompted a fair degree of uncertainty in connection with the possible formation of metastable phases. Under some curing conditions such phases may evolve into stable cubic phases, generating greater volume and porosity, with the concomitant adverse effects on blended cement mechanical performance and durability (Silva and Glasser, 1993).

Research has focused on the use of kaolinite (K)-based clay minerals which when heated to temperatures of 400 °C to 700 °C originate metakaolinite (MK) (Kakali et al., 2001; Fabbri et al., 2013; Bich et al., 2009). Further to research conducted by Ptacek et al. (2014), K converts to MK in three stages: lamination, dehydroxylation and MK formation. The sequential order of the first two depends directly on the activation rate. As MK exhibits high pozzolanicity, it is ideal for use as a supplementary cementitious material in commercial blended cement manufacture (Siddique and Klaus, 2009; Rashad, 2013) as acknowledged in international standards (European Standard, 2011).

A number of authors (Murat, 1983; Serry et al., 1984; Santos et al., 2014; Frías and Cabrera, 2001) have shown that the main hydrated phases resulting from the pozzolanic reaction in pure MK/lime systems at ambient temperature are C-S-H gels, C_4AH_{13}, C_2ASH_8 (strätlingite) and $C_4A_CH_{11}$. The amount of each phase formed depends on factors such as the MK/lime and MK/binder ratios, hydration time and curing humidity. The implications of the presence of these hydrated phases in the cementitious matrix include a decline in microporosity (Frías and Cabrera, 2000; Mleza and Hajjaji, 2012; Sabir et al., 2001; Jiang et al., 2015), which has a direct impact on physical-mechanical properties and durability. Higher curing temperatures, in turn, are known to favour the

formation of the (variable composition) cubic hydrogarnet phase (C_3AH_6-$C_3AS_3H_n$) (Klimesch and Ray, 19989; Rios et al., 2009; Cabrera and Frías, 2001; Martínez and Frías, 2011).

The study of the effect of temperature on pozzolanic reactions in cement matrices dates back to the nineteen nineties, when Silva et al. (1993) reported that in high-lime matrices C-S-H gels and hydrogarnet are stable up to temperatures of 55 °C. In contrast, metastable phases C_2ASH_8 and C_4AH_{13} destabilise at that temperature, ultimately forming a stable cubic hydrogarnet. Those developments induce a decline in matrix volume of nearly 13 %, with a rise in porosity and concomitant loss of strength. Amboise and Murat (1985) established the possible chemical reactions for phase formation and evolution, as follows:

$$2AS_2 + 9CH + 12H \rightarrow C_2ASH_8 + C_4AH_{13} + 3CSH$$

$$C_2ASH_8 + C_4AH_{13} \rightarrow 2C_3AS_{0.5}H_5 + 11H$$

With a view to obtaining a fuller understanding of these reactions at longer times in pure MK/lime systems, Martínez and Frías (2011), Frías and Cabrera (2002), Frías and Sánchez de Rojas (2003) and Frías et al. (2003) studied a (1:1 by weight) MK/lime system at 60 °C for 123 d. According to their findings, metastable hexagonal phases co-existed with a stable cubic phase resulting from the pozzolanic reaction in a medium with traces of $Ca(OH)_2$. At that curing age (123 d), nearly all the metastable phases had evolved into stable hydrogarnet phases, with a perceptible decline in C-S-H gel concentration. Pesce et al. (2014) reported similar findings for 28 day MK/lime blends cured at 25 °C, with the formation of C-S-H gels, C_4AH_{13} and $C_2ASH_{6,}$. These authors

78   also observed a higher concentration of cubic phase C_3ASH_6 and a lower C-S-H gel

79   content relative to other systems studied.

80   At longer times (5 years), Frías (2006a) showed hexagonal metastable C_2ASH_8 and

81   stable cubic hydrogarnet to be the predominant crystalline hydrated phases in a

82    $Ca(OH)_2$-free MK/lime system (1:1 by weight), along with traces of vertumnite

83   ($Ca_4Al_4Si_4O_6$ $(OH)_{24}$ $3H_2O$), a strätlingite polytype differing from the general form in

84   its silicon and water content (Rinaldi et al., 1990).

85   Whilst today's civil works are designed to a service life of over 100 years, no scientific

86   studies on the evolution of these MK/lime mineralogical phases under such extreme

87   curing conditions at longer curing times have yet been forthcoming. This article

88   describes a first-time study of the mineral phases present in MK/lime systems cured at

89   60 °C for 15 years. The findings, which further the scientific understanding of the

90   pozzolanic reaction in aluminosilicate systems, will have a direct impact on the

91   properties of cementitious systems and consequently their possible applications in

92   engineering.

93

94   **2.   EXPERIMENTAL PROCEDURES**
95   **2.1   Materials**

96   A commercial metakaolin (MK) manufactured in the UK was used in this study. The

97   XRF determined elemental composition in Table 1 shows that the MK used consisted

98   primarily in Si and Al. Its BET specific surface was found to be 15 m^2/g. XRD analysis

99   (spectrum not shown) revealed the presence of traces of quartz and mica. Analytical

100   grade lime $Ca(OH)_2$ was used.

101

102   **2.2   Blended MK-Ca(OH)$_2$ pastes**

103   The blended pastes were prepared by mixing a 1:1 (by weight) ratio of MK and lime

104   with water at a water/solid ratio of 2.37. The resulting slurry was placed in a lidded

105   plastic airtight container and submerged in water at 60 °C for 15 years as depicted in the

106   sketch in Figure 1.

107   After the 15 year curing, the solid paste was removed from the container, mixed with

108   acetone and heated in a laboratory oven at 40 °C for 24 h to detain the pozzolanic

109   reaction.

110

111   ## 2.3 Instrumental techniques

112   The mineralogical composition of the bulk samples was determined by X-ray powder

113   diffraction (XRD) on a Siemens D-5000 (Munich, Germany) X-ray diffractometer fitted

114   with a Cu anode, as well as a 2.0 mm divergence and a 0.6 mm reception slit. The

115   operating settings were 30 mA, 40 kV; scanning at 0.041° (2θ) steps; count time, 3 s.

116   Rietveld analysis was performed using rutile as the internal standard to quantify the

117   amorphous phase (Rietveld, 1969; Ruan and Ward, 2002). The quantification findings

118   also specified the X^2 goodness of fit, which compared peak intensities calculated from

119   the spectrum to the experimental values based on phase weight. Although ideally X^2

120   should be equal to 1, since the discrepancies between the observed and calculated data

121   widen substantially in materials containing over three phases, values of $X^2 < 10$ are

122   generally accepted as indicative of valid results.

123   Sample morphology and microanalysis were determined on a Thermo Fisher Scientific

124   (FEI Company) Inspect scanning electron microscope (Hillsboro, OR) equipped with an

125   X-ray dispersive analyser. Chemical composition was computed as the average of ten

126   analyses per sample, ± the resulting standard deviation. The findings are expressed in

127   wt% of oxides.

128 Raman spectra were recorded on a Renishaw inVia confocal Raman spectroscope fitted

129 with a Leica microscope and an electrically refrigerated CCD camera. The instrument's

130 diode laser delivered a 785 nm excitation frequency and a 25 mW laser beam that was

131 focused on a quartz tube containing the sample. Silicon was used to calibrate the

132 frequencies.

133 The ^{27}Al and ^{29}Si MAS NMR spectra were recorded with a Bruker MLS-400

134 spectrophotometer operating at 79.49 mHz. The recording conditions for the ^{27}Al

135 spectra were: spinning speed, 10 kHz; pulse width, 2 µs; relaxation delay, 5 s; No.

136 scans, typically 360. The conditions for the ^{29}Si spectra were spinning speed, 10 kHz;

137 pulse width, 5 µs; relaxation delay, 20 s; No. scans, typically 1120. Tetramethylsilane

138 was used as a reference for the ^{29}Si and a 0.1 M aqueous solution of Al $(NO_3)_3$ for the

139 ^{27}Al chemical shifts. The 600 ^{27}Al CP-MAS scans made to generate the spectrum were

140 recorded at a contact time of 10 ms.

141 Fourier transform infrared (FTIR) analysis was conducted on a Thermoscientific Nicolet

142 6700 (Waltham, USA) spectrometer. One-mg samples pressed into 300 mg of KBr were

143 analysed in spectral range 4000 cm^{-1} to 400 cm^{-1}.

144 Thermogravimetric and differential thermal analyses (TG/DTA) were run on a Stanton

145 STA 781 instrument. Samples weighing 30 mg to 35 mg were heated at a rate of 10

146 ºC/min in a nitrogen atmosphere.

147 3. RESULTS

148 3.1 XRD-determined mineral phases

149 The 15 year XRD spectrum for MK/Ca(OH)$_2$ exhibited diffraction lines for three

150 CaCO$_3$ polymorphs (calcite, aragonite and vaterite) and gismondine (Figure 2). Calcite

151 was identified in the calcium carbonate group by reflections at 3.85 Å (23.1 2θ); 3.03 Å

152 (29.4 2θ); 2.49 Å (35.9 2θ); 2.28 Å (39.5 2θ) 2.09 Å (43.2 2θ); 1.92 Å (47.3 2θ) and

153 1.87 Å (48.6 2θ); aragonite at 3.39 Å (26.3 2θ); 3.27 Å (27.2 2θ); 2.73 Å (32.8 2θ);

154 2.70 Å (33.12θ); 1.81 Å (50.4 2θ); 1.74 Å (52.5 2θ) and 1.72 Å (53.2 2θ); and vaterite

155 primarily at 4.20 Å (21.1 2θ) and 3.57 Å (24.9 2θ). Gismondine was identified by

156 reflections at 9.98Å (8.85 2θ); 7.26 Å (12.14 2θ); 5.95 Å (14.85 2θ); 5.74Å (15.4 2θ);

157 5.01 Å (17.69 2θ); 4.90 Å (18.1 2θ); 4.45 Å (19.9 2θ); 4.26 Å (20.82 2θ); 3.36 Å (26.5

158 2θ); 3.18 Å (28.01 2θ); 3.12 Å (28.58 2θ); 2.74 Å (32.62 2θ); 2.66 Å (33.64 2θ) and

159 206 Å (43.9 2θ).

160

161 The Rietveld quantification of the mineral phases yielded the following results:

162 gismondine 30 %, aragonite 20 %, calcite 20 %, vaterite 6 % and amorphous phase

163 24 % ($X^2 = 3.7$). The sharp, narrow reflections for gismondine, aragonite and calcite

164 denoted a high degree of crystallisation. The presence of possible traces of non-

165 crystalline strätlingite and hydrogarnet could also be inferred from the low humps in the

166 baseline in the areas of the spectrum associated with their characteristic reflections:

167 respectively 12.6 Å (7.1 2θ)) and 2.8 Å (31.9 2θ). These two phases have been

168 identified as the main pozzolanic reaction products in 5 year materials (Frías, 2006a).

169

170 **3.2 SEM/EDX-determined mineral phases**

171 The elemental analysis of the various morphologies revealed by the textural study is

172 given in Table 2. Further to the combined SEM/EDX information, the morphologies

173 and mineral phases present were as follows.

174 Hexagonal plates and some crystallisation were observed on the conglomerate, which

175 served as a substrate (Table 2 and Figure 3). The plate surfaces were eroded and highly

176 porous while their edges were poorly defined and rounded, possibly denoting incipient

177 degradation. EDX microanalysis (Table 2) identified the plates as metastable phases

178 C_4AH_{13} (Figure 3a) and strätlingite (Figure 3b).

179 The conglomerates observed in the sample exhibited scantly defined morphologies:

180 skeletal forms with rounded edges and pock-holed surfaces (Figures 3 to 5 and Table 2).

181 They consisted primarily in silica and alumina with smaller proportions of sodium,

182 potassium and magnesium, with substantial quantities of randomly scattered calcium.

183 The appearance and composition of this sand were indicative of time-induced

184 degradation of the other materials present, such as C-S-H gels, C_4AH_{13}, strätlingite and

185 hydrogarnets.

186 Substantial numbers of fibres with a composition similar to that of C-S-H gel were

187 observed to form on the conglomerates (Figure 4a and Table 2). Calcium feldspar

188 crystals also formed (Figure 4b and Table 2), with smooth surfaces and well-defined

189 grain edges as a result of heterogeneous nucleation on the conglomerate substrate.

190 The conglomerate also served as a crystallisation substrate for calcium carbonates and

191 cubic calcium zeolites of the gismondine/garronite family. The calcium carbonate

192 crystals were the result of one of two processes: a) neo-formation of calcium carbonates

193 characterised by smooth surfaces and sharp grain edges (Figure 4c) and b) deterioration

194 of the calcium carbonates present in the starting paste, attested to by the rough surfaces

195 and poorly defined edges of the crystals (Figure 4d).

196 Gismondine, a calcium zeolite, exhibited a pseudo-cubic morphology ($P2_1/c$ symmetry),

197 pseudo-octahedral clustering and a Si/(Si+Al) ratio of close to 0.5 (Fischer and

198 Schramamm, 1971). Its grain edges were well defined and its surfaces smooth,

199 indicating neo-formation (Figure 5a and Table 2). The calcium garronite in turn

200 (Figure 5b) consisted in compact radial conglomerates with Si/(Si+Al) ratios of over

201 0.5, rough surfaces and poorly defined crystal edges. Such poorly defined edges did not

202 denote degradation in this case, however, for garronite initially generates a disorderly

203 phase that over time tends to partial order and a scantly defined morphology. Its

204 structure exhibited four orientation domains and $I4_1/amd$ symmetry (Gottardi et al.,

205 1974) (Figure 5b and Table 2).

3.3 Micro-Raman-determined mineral phases

207 The Raman spectrum for the MK/lime sample (Figure 6) contained signals

208 characteristic of calcite (1087 cm^{-1}, 712 cm^{-1} and 280 cm^{-1}) and three wide signals at

209 $990 \text{ cm}^{-1,}$ 660 cm^{-1} and 445 cm^{-1}, attributable to the network vibrations in zeolites. The

210 first of the bands was assigned to Si-O stretching vibrations, the second to T-O

211 symmetrical stretching vibrations and the third to the vibrations generated by the T-O-T

212 bonds in aluminosilicates, probably with a four tetrahedral ring (Dutta and Barco,

213 1988). The gismondine observed in the XRD and SEM analyses were a likely source of

214 such vibrations. The spectrum also contained a wide signal at 360 cm^{-1} to 316 cm^{-1}

215 assignable to Ca-O vibrations. The wide signal at 860 cm^{-1} to 825 cm^{-1} appearing in

216 some types of zeolites is due to the Si-O vibrations in their terminal Si atoms. The

217 widening of the band peaking at 1087 cm^{-1} (calcite) might denote the presence of

218 amorphous calcium carbonate (not identified by XRD) or of carbonate phases such as

219 monocarboaluminate.

220

3.4 ^{29}Si and ^{27}Al NMR-determined mineral phases

222 The ^{27}Al MAS NMR spectrum for the 15 year MK/lime sample reproduced in Figure 7a

223 showed a very intense tetrahedral Al signal (54.9 ppm) with a pentahedral Al shoulder

224 (25 ppm to 45 ppm) and a second signal attributed to octahedral Al (6.4 ppm). Since

225   according to Richardson et al. (2010) Q^3 bridging sites across the interlayer generate a

226   resonance peaking at around 58 ppm, the signal at 54.9 ppm was attributed to

227   tetrahedrally coordinated aluminium in aluminosilicate (gismondine) (Khodabandeh and

228   davis, 2006). Anderson et al. (2006) identified a low-frequency peak at 35 ppm as an

229   aluminate phase associated with an amorphous or scantly crystalline aluminate

230   hydroxide, which would account for the shoulder observed here. The presence of the

231   octahedral Al signal at 6.4 ppm denoted Al replacement of Si in both the tetrahedral and

232   octahedral sheets in the zeolite's layered silicate structure.

233   The ^{29}Si NMR spectrum (Figure 7b) exhibited two signals, one very intense peaking at

234   90 ppm and the other less intense, peaking at 94 ppm, both in the interval characteristic

235   of Q^3 units. No signals were observed in the Q^1, Q^2 unit interval, which would be

236   indicative of the presence of C-S-H gels forming during cement hydration or the

237   pozzolanic reaction between MK and lime. That confirmed the Raman and XRD

238   findings suggesting C-S-H gel disintegration and the formation of a gismondine-like

239   zeolite.

240

241   **3.5 FT-IR determined mineral phases**

242   The bands at 1008 cm^{-1} and 439 cm^{-1} observed on the FTIR spectrum for the 15 year

243   MK/lime paste (Figure 8) were due to the internal vibrations in TO_4 tetrahedra (T = Al,

244   Si). The former was associated with T-O bond asymmetrical stretching vibrations and

245   the latter to T-O bond internal bending vibrations (Andersen et al., 2006). Both T-O

246   bonds were present in the mineral phases identified. The intermediate intensity signal

247   peaking at 580 cm^{-1} was assigned to zeolite external ring vibrations.

248   The IR spectrum also exhibited a very intense signal peaking at 1470 cm^{-1} attributed to

249   CO_3 ν_3 asymmetric stretching vibrations generated by the carbonates in aragonite. The

250   signals at 874 cm^{-1} and 855 cm^{-1} were due to CO_3 ν_2 asymmetric bending vibrations

251 induced by calcite and aragonite, respectively. Similarly, the signals at 712 cm^{-1} and

252 700 cm^{-1} were respectively attributed to calcite and aragonite CO_3 ν_1 symmetric

253 bending (Gunasekaran et al., 2006). The presence of vaterite, which according to the

254 XRD findings accounted for 6 % of the sample, was detected as a shoulder at 745 cm^{-1},

255 confirming its low concentration. FT-IR likewise confirmed zeolite and carbonate

256 polymorph formation. The signals at 580 cm^{-1} and 438 cm^{-1} were associated with AlO_6

257 units, possibly indicative of a monocarboaluminate hydrate phase, which would

258 corroborate the Micro-Raman data.

259
260 **3.6 TG/DTA-determined mineral phases**
261
262 The TG thermogram for the paste (Figure 9) showed a total loss of 30.41 % across the

263 test interval (25 °C to 1000 °C), in which two substantial areas of weight loss could be

264 clearly identified. A loss of 9.34 % of the total was recorded in the lower (25 °C to

265 300 °C) and of 16.84 % loss in the higher (635 °C to 789 °C) temperature range. The

266 DTA curve clearly showed five endothermal peaks in the former, the most intense of

267 which at 146.7 °C and the four others at 50 °C, 93 °C, 110 °C and 231 °C. The 50 °C

268 endothermal peak represented the loss of adsorbed moisture while the others were

269 associated with dehydroxylation of the mineral phases present in the 15 years sample.

270 According to the literature (Frías, 2006b; Foldvari, 2011), the main hydrated phases

271 resulting from the MK/lime pozzolanic reaction dehydroxylate in this temperature

272 interval: C-S-H gel at 110 °C to 140 °C, C_2ASH_8 at 140 °C to 160 °C, C_4AH_{13} at 170 °C

273 to 200 °C, carboaluminate at 200 °C to 230 °C.

274 The presence of feldspar and zeolites, primarily gismondine, was confirmed by the

275 endothermal peaks at 88 °C to 115 °C, 115 °C to 208 °C and 208 °C to 290 °C,

276 representative of the consecutive loss of water molecules (0.5, 1.5 and 0.5 moles,

277   respectively). Given endothermal peak overlapping, they could not be clearly assigned

278   to any specific mineral phase.

279   The second interval exhibited a wide endothermal signal peaking at 762 °C, typical of

280   carbonate decarbonation in the $CaCO_3$ polymorphs identified by XRD, i.e., primarily

281   calcite, aragonite and some vaterite. The presence of carbonates was related to

282   carbonation of the portlandite in the $MK/Ca(OH)_2$ system over the 15 year curing,

283   storage and testing period.

284

285   **4.   DISCUSSION**

286   Stratlingite, C_4AH_{13}, hydrogarnet and C-S-H gels are the majority short- and medium-

287   term hydrated phases in pozzolanic reactions taking place at 60 °C (Martínez and Frías,

288   2011; Frías and Cabrera, 2002; Frías and Sánchez de Rojas, 2003; Frías et al., 2013).

289   According to Silva et al. (1993) [1], hexagonal phases C_2ASH_8 and C_4AH_{13} are

290   metastable, evolving under high temperature and humidity conditions toward a stable,

291   hydrogarnet family phase with variable compositions. This study showed for the first

292   time that exposure time plays a significant role even for stable mineral phases, a finding

293   not experimentally proven to date. Over the 15 years of exposure, all the (stable and

294   metastable) hydration phases evolved toward carbonates, feldspars and zeolites due to

295   degradation and heterogeneous nucleation.

296   Hydrogarnets, part of the nesosilicate family, constitute an isostructural group in the

297   cubic system with the general formula $(SiO_4)_3A_3B_2$, where A represents divalent cations

298   such as calcium, magnesium, iron or manganese and B trivalent cations such as

299   aluminium, iron or chromium. Hydrated hydrogarnets also contain water molecules in

300   their structure in the form of $(OH)^{4-}$ groups, with the four hydrogen atoms replacing a

301   silicon atom in the $(SiO_4)^{4-}$ tetrahedron. The crystalline divalent cations exhibit

302 dodecahedral, the trivalent cations octahedral and the silicon tetrahedral coordination.

303 Calcium silicate hydrate (C-S-H), strätlingite ($2CaO.Al_2O_3.SiO_2.8H_2O$) and a

304 hydrogarnet ($3CaO.Al_2O_3.6H_2O$)-katoite ($3CaO.Al_2O_3.SiO_2.4H_2O$) solid solution may

305 co-exist in cements.

306 In strätlingite, aluminium atoms are tetrahedrally or octahedrally coordinated and

307 silicon atoms exist predominantly as Q^2, Q^2 (1Al) or Q^2 (2Al) units. In 1976, Kuzel

308 (1976) described strätlingite structure based on the formula: $[Ca_2Al^{VI} (OH)_6]$

309 $[Al^{IV}SiO_3(OH)_2(H_2O)_4]$, indicating that the Al^{IV}/Al^{VI} ratio was equal to 1. Muller et al.

310 (1986) in turn determined the silicon in strätlingite to constitute a Q^3 (3Al) unit.

311 Strätlingite structure may be affected by the presence of alkalis, which significantly

312 reduce the Al^{IV}/Al^{VI} ratio. This mineral consists in a brucite-like octahedral layer

313 comprising calcium and aluminium with an ideal composition of $[Ca_2Al (OH)_6 .2H_2O]^+$

314 and a double tetrahedral layer with ideal composition $[(T,\square)_4(OH,O)_8 \ 0.25 \ H_2O]$.

315 Rinaldi et al. 1990) observed that the tetrahedral positions could be occupied by silicon

316 or aluminium ions and that 45 % of those positions in the double tetrahedral layer were

317 vacant. The calcium atoms were hepta-coordinated and occupied cationic positions

318 associated with the octahedral aluminium layer. The water molecules, most found in the

319 octahedral layer and projecting into the centre of the rings comprising the double

320 tetrahedral layers, hold the tetra and octahedral layers together by forming hydrogen

321 bonds. One additional water molecule is located in the centre of each tetrahedral ring.

322 The dimensions of the unit cell infer overlapping in three octahedral layers and three

323 interlayers (double tetrahedral layers) in direction [001] (Rinaldi, 1990). The degree of

324 structural disorder in the strätlingite microstructure forming in the cement pastes, which

325 depends essentially on the hydration conditions (Santacruz et al., 2016), must have

326 been substantial, for greater disorder would favour degradation.

327 The loosely organised structure of C-S-H gel hinders its characterisation with XRD. It

328 has nonetheless been shown to have a laminar crystalline structure similar to two

329 minerals: tobermorite, when the Ca/Si ratio ranges from 0.66 to 1.5, and jennite, when it

330 is over 1.5. The nanometer-scale laminar thickness (Santacruz et al., 2016) of this C-S-

331 H gel affects the mechanical and engineering properties of cements and concretes

332 Ioannidouk et al., 2016). When the Ca/Si ratio = 0.6, C-S-H gel structure consists in a

333 double central sheet of six or seven calcium ions linked to oxygen ions connected on

334 each side to chains of silica tetrahedra. The silicate chain adopts a dreierketten

335 arrangement, i.e., a repeating unit consisting in three SiO4 tetrahedra, one bridging and

336 two pairing. The latter two share oxygen atoms with a sheet of octahedral CaO while

337 the former does not. All the unattached oxygen atoms in the silicate chain are

338 protonated as hydroxyls. The interlayer space is occupied by water molecules and, if the

339 Ca/Si ratio is > 0.83, by calcium ions (Bonaccorsi et al., 2004). The main difference

340 between C-S-H gel and tobermorite / jennite is that in the former the chains are finite

341 and in the latter two infinite. The evolution of C-S-H gel structure is governed by the

342 Ca/Si ratio. If the ratio is 1.5, the protons in the bridging SiO_4 tetrahedra in the

343 drierketten units are progressively replaced with calcium ions, which are taken up in the

344 hydrated interlayer space. If the Ca/Si ratio declines to values of around 1.0, the degree

345 of chain polymerisation declines and the hydroxyl groups are ionised, whereby the

346 negative charge in the laminas is maintained and the calcium ions in the interlayer

347 remain unaffected (Nachbaur et al., 1998).

348 The structures of the materials described may be deemed to consist in mixes of surface

349 groups. The calcium ion concentration and pH in the solution are known to ultimately

350 induce calcium ion supersaturation (Madani et al., 1990). Four types of surface groups

351 may form: SiOH, SiO⁻, $SiOCa^+$ and SiOCaOH, the first two at low and the last two at

352 higher Ca concentrations. The latter condition induces high proportions of reactive

353 $SiOCa^+$ positions. Such differential surface reactivity depending on pH and especially

354 Ca availability might explain the present observations: the ready nucleation and growth

355 of calcium feldspars and gel fibres on low-calcium substrates (with SiOH and SiO^-

356 surface groups) and the formation of calcium carbonates and zeolites on high-calcium

357 substrates ($SiOCa^+$ and SiOCaOH).

358 Zeolites may form via hydrothermal synthesis of MK and lime in the presence of high

359 concentrations of tetra- and penta-coordinated aluminium and a minimum content of

360 hexa-coordinated Al (Ferro et al., 2002). The presence of three forms of coordinated

361 aluminium observed with NMR might explain zeolite nucleation and growth on a

362 substrate consisting in high-calcium conglomerate. Such conditions would suffice for

363 the formation of zeolitic calcium (gismondine), a double chain zeolite with four

364 interconnected rings exhibiting slightly deformed P21/c symmetry and tetrahedra with

365 centres alternatively occupied by Si or Al. Ca in turn is located on one of the four

366 bending positions that connect two tetrahedral oxygens to water molecules, distributed

367 across six positions (Fischer and Schramm, 1971).

368 The sketch in Figure 7 shows how gismondine would nucleate via the cycling of double

369 tetrahedral chains resulting from the disintegration of the initial mineral phases

370 (strätlingite, C_4AH_{13}, C_2ASH_8, hydrogarnets and C-S-H gel). In Si gismondine the Al

371 distribution is orderly and only one type of extra-framework cation (calcium) is present

372 in the channels. Extra-framework cations are a determinant in the mechanism governing

373 zeolite deformation Madani et al., 1990), while polyhedral coordinated Ca serves as a

374 template that also drives framework deformation (Fois et al., 2005; Betti et al., 2007).

375 Zeolite formation as observed in cementitious systems has also been described in

376 cement- and lime-free media, such as in geopolymer synthesis, where it occurs along

377 with amorphous phase generation (Davidovits, 2008). The chemical composition of

378 geopolymers is similar to that of C-S-H gel and zeolite-like materials. Some authors

379 have described geopolymers as zeolite precursors (Liew, 2016). Zeolite crystallization is

380 favoured by high water content, high curing temperature and lengthy curing periods

381 (Provis, 2005). The number of zeolite crystallites also grows with time (Duxson et al.,

382 2005).

383 The results of this study show that exposing lime- and pozzolan-based cementitious

384 matrices to high temperatures for long curing times induces mineralogical

385 transformations that primarily induce zeolite formation. That process, due to a high

386 calcium concentration and high pH that favour the formation of $SiOCa^+$- and SiOCaOH-

387 like, zeolite-seeding surface groups, entails the cycling of the double chain in C-S-H gel

388 and concomitant gismondine formation.

389 The generally accepted notion that metastable phases may co-exist at high curing

390 temperatures and evolve thermodynamically toward a stable phase may therefore be

391 true, albeit only partially, for the experimental trials conducted to date cover relatively

392 short hydration periods. The present results reveal that over much longer curing times

393 such phases practically disappear and give way to others, suggesting new lines of

394 research for the international scientific community.

395 **5. CONCLUSIONS**

396 In this work the reaction between metakaolinite and calcium hydroxide at 60ºC after 15

397 years was studied. Although it is known that stable and metastable phases coexist at

398 times less than 5 years, the formation of gismondine-type zeolites occurs at longer

399 hydration times.

400 Microstructurally, aggregates from the degradation of the initial compounds C-S-H,

401 C_4AH_{13}, stratlingite and hydrogarnets were observed, which serve as crystallization

402 substrates for new phases such as calcite and mainly calcium zeolites of the gismondine

403 type. The presence of these phases is confirmed by characterization techniques such as

404 XRD, Micro-Raman, FT-IR and ^{27}Al and ^{29}Si NMR.

405 The formation of calcium zeolite, gismondine, is postulated that occurs by cycling

406 double chains of the initially formed C-S-H gel. This shows the formation of zeolites in

407 systems with lime, as currently has only been described in geopolymeric systems, with

408 high alkali content.

409 This new understanding will have a direct impact on the manufacture of metakaolinite-

410 blended cements and their engineering properties, for the structures engineered today

411 are designed for a future service life of 100 to 200 years.

412

413 **ACKNOWLEDGEMENTS**

416 **REFERENCES**

417 1. Ambroise, J., Murat, M., Pera. J., 1985. Hydration reaction and hardening of
418   calcined clays and related mineral. VI. Experimental conditions for strength. Cem.
419   Concr. Res. 15, 83-88.
420 2. Andersen, M.D., Jakobsen, H.J., Skibsted, J., 2006. A new aluminium-hydrate
421   species in hydrated Portland cements characterized by 27Al and 29Si MAS NMR
422   spectroscopy. Cem. Concr. Res. 36, 3-17
423 3. Betti, C., Fois, E.,, Mazzucato, E., Medici, C., Quartieri, S., Tabacchi, G.,
424   Vezzalini, G., Dmitriev, V., 2007. Gismondine under HP: Deformation mechanism
425   and reorganization of the extra-framework species. Micropor. Mesopor. Mater, 103,
426   190-209.
427 4. Bich, Ch., Ambroise, J., Pera, J., 2009. Influence of degree of dehydroxilation on
428   the pozzolanic activity of metakaolin. Appl. Clay Sci., 44, 194-200.
429 5. Bonaccorsi, E., Merlino, S., Taylor, H.W., 2004. The crystal structure of jennite,
430   Ca9Si6O18(OH)6·8H2O. Cem.Concr. Res. 34, 1481-1488.
431 6. Cabrera, J., Frías, M., 2001. Mechanism of hydration of the MK-lime-water system.
432   Cem. Concr. Res., 31, 177-182.
433 7. Davidovits, J. Geopolymer chemistry and applications. (2nd ed.), Institute
434   Geopolymere, 16 rue Galilee, 02100 Saint Quentin, France; 2008
435 8. De Silva, P.S., Glasser, F.P., 1993. Phase relations in the system CaO-Al$_2$O$_3$-SiO$_2$-
436   H$_2$O relevant to MK-Calcium Hydroxide. Cem. Concr. Res., 23, 627-639.

437   9. Dutta, P.K., Del Barco, B., 1988. Raman Spectroscopy of Zeolite A: Influence of
438   Si/AI Ratio. J. Phys. Chem., 92, 354-357.
439   10. Duxson, P., Provis, J.L., Lukey, G.C., Separovic, F., Jannie, S.J., van Deventer,
440   J.S.V., 2005. 29Si NMR Study of Structural Ordering in Aluminosilicate
441   Geopolymer Gels. Langmuir, 21, 3028–3036
442   11. European Standard, 2011. EN-197-1:2011. Composition, specification and
443   conformity criteria for common cements.
444   12. Fabbri, B., Gualtieri, S., Leonardi, C., 2013. Modifications induced by the thermal
445   treatment of kaolin and determination of reactivity of metakaolin. Appl. Clay Sci.,
446   73, 2-10.
447   13. Ferro, O., Quartieri, S., Vezzalini, G., Fois,, E., Gamba, A., Tabacchi, G., 2002.
448   High-pressure behaviour of yugawaralite at different water content: an ab initio
449   study. Am. Mineral, 87,1415-1423.
450
451   14. Fischer, K., Schramm, V., 1971. Crystal structure of gismondite, a detailed
452   refinement. In: Molecular sieve zeolites. Adv. Chem. Ser., 101, 250-258.
453   15. Foldvari, M., 2011. Handbook of thermogravimetric system of minerals and its use
454   in geological practise. Geological Institute of Hungary, Budapest.
455   16. Fois, E., Gamba, A., Tabacchi, G., Arletti, R., Quartieri, S., Vezzalini, G., 2005.
456   The template effect of the extra-framework content on zeolite compression: The
457   case of yugawaralite. Am. Mineral, 90, 28-35.
458   17. Frías, M., Cabrera, J.,2001. Influence of MK on the reaction kinetic in MK/lime
459   and MK/blended cement systems at 20ºC. Cem. Concr. Res., 31,519-527.
460   18. Frías, M., Cabrera, J., 2000. Pore size distribution and degree of hydration of MK-
461   cement pastes. Cem. Concr. Res., 30, 561-560.
462   19. Frías, M., Cabrera, J., 2002.The effect of temperature on the hydration rate and
463   stability of the hydration phases of MK-lime-water systems. Cem. Concr. Res., 32,
464   133-138.
465   20. Frías, M., Sánchez de Rojas, M.I.,2003. The effect of high curing temperature on
466   the reaction kinetics in MK/lime and MK/blended cement matrices at 60ºC. Cem
467   Concr Res., 33, 643-649.
468   21. Frías, M., Martínez, S., Blasco, T., Frías-Rodríguez, M., 2013. Evolution of
469   mineralogical phases by 27Al and 29Si NMR in MK-Ca(OH)2 system cured at
470   60ºC. J. Am. Ceram. Soc., 96, 2306-2310
471   22. Frías, M.,2006a. Study of hydration phases present in a MK-lime system cured at
472   60ºC and 60 months of reaction. Cem. Concr. Res., 36, 827-831.
473   23. Frías, M., 2006b. The effect of MK on the reaction products and microporosity in
474   blended cement pastes submitted to long hydration time and high curing
475   temperature. Adv. Cem. Res., 18, 1-6.
476   24. Gbozee, M., Zheng, K., He, F., Zeng, X., 2018. The influence of aluminium from
477   metakaolin on chemical binding of chloride ions in hydrated cement pastes. Appl.
478   Clay. Sci., 158,186-194.
479   25. Gottardi G, Alberti A. Domain structure in garronite: a hypothesis. Miner Mag.
480   1974; 39: 898-899
481   26. Gunasekaran S, Anbalagan G, Pandi S. Raman and infrared spectra of carbonates of
482   calcite structure. J. Raman Spectrosc. 2006; 37: 892-899

483   27. Jiang G, Rong Z, Sun W. Effects of MK on mechanical properties, pore structure
484   and hydration heat of mortars at 0.17 w/b ratio. Constr Build Mater. 2015; 93: 564-
485   572.
486   28. IoannidouK., Kanduc M, Li L, Frenkel D, Dobnikar J, Diel Gado E. The crucial
487   effect of early stage gelation on the mechanical properties of cement hydrates. Nat.
488   Commun. 7:12106 (2016).
489   29. Kakali G, Perraki T, Tsivilis S, Badogiannis E. Thermal treatment of Kaolin: the
490   effect of mineralogy on the pozzolanic reactivity. Appl Clay Sci. 2001; 20: 73-80.
491   30. Khodabandeh S, Davis ME. Alteration of perlite to calcium zeolites. Microporous
492   Materials 1997; 9:161-172
493   31. Klimesch DS, Ray A. Hydrogarnet formation during autoclaving at 180ºC in
494   unstirred MK-lime-quartz slurries. Cem Concr Res. 1998; 28:1109-1117
495   32. Kuzel H. Crystallographic Data and Thermal Decomposition of Synthetic Gehlenite
496   Hydrate 2CaO·Al2O3·SiO2·8H2O. Neues Jahrb Mineral Monatsh. 1976; (7):
497   319–326.
498   33. Liew Y M, Heah ChY, Mohd A B, Kamarudin H. Structure and properties of clay-
499   based geopolymer cement: A review. Progress in Materials Science 2016; 83: 595-
500   629
501
502   34. Madani A, Aznar A, Sanz J, Serratosa JM. Silicon-29 and aluminum-27 NMR
503   study of zeolite formation from alkali-leached kaolinites: influence of thermal
504   preactivation. J Phys Chem. 1990; 94: 760-768
505   35. Martínez S, Frías M. Micro-raman study of stable and metastable phases in
506   MK/Ca(OH)2 system cured at 60ºC. Appl Clay Sci. 2011; 51: 283-286
507   36. Mleza Y, Hajjaji M. Microstructural characterization and physical properties of
508   cured thermally activated clay-lime blends. Constr Build Mater. 2012; 26: 226-232.
509   37. Muller D, Gessner W, Samoson A, Lippmaa E, Scheler G. Solid-state 27Al NMR
510   studies on polycrystalline aluminates of the system CaO-Al2O3. Polyhedron 1986;
511   5: 779-785.
512   38. Murat M. Hydration reaction and hardening of calcined clays and related minerals.
513   Cem Concr Res. 1983; 13: 259-266
514   39. Nachbaur L, Nkinamubanzi PC, Nonat A, Mutin JC. Electrokinetic Properties
515   which Control the Coagulation of Silicate Cement Suspensions during Early Age
516   Hydration. J Colloid Interface Sci. 1998; 202: 261-268.
517   40. Pesce GL, Bowen CR, Rocha J, Sardo M, Allen GC, Walker PJ, Denuault G,
518   Serrapede M, Ball RJ. Monitoring hydration in lime-MK composites using
519   electrochemical impedance spectroscopy and nuclear magnetic resonance
520   spectroscopy. Clay Minerals2014; 49: 341-358.
521   41. Provis JL, Lukey GC, van Deventer JSJ. Do geopolymers actually contain
522   nanocrystalline zeolites? A reexamination of existing results. Chem Mater. 2005;
523   17: 3075-3085
524   42. Ptacek P, Frajkorova F, Soukal F, Opravil T. Kinetics and mechanism of three
525   stages of thermal transformation of kaolinite to metakaolinite. Powder Technology
526   2014; 264: 439-445.
527   43. Rashad AM. Metakaolin as cementitious material: History, scours, production and
528   composition. A comprehensive overview. Constr Build Mater. 2013; 41: 303-318.

529 44. Richardson IG, Skibsted J, Black L, Kirkpatrick RJ. Characterization of cement
530   hydrate phases by TEM, NMR and Raman spectroscopy. Adv Cem Res. 2010; 22:
531   233-248
532 45. Ríos CA, Willians CD, Fullen MA. Hydrotermal synthesis of hydrogarnet and
533   tobermorite at 175ºC from kaolinite and metakaolinite in the Cao-Al2O3-SiO2-
534   H2O system: A comparative study. Appl Clay Sci. 2009; 43: 228-237.
535 46. Rietveld HM. A profile refinement method for nuclear and magnetic structures. J.
536   Appl. Crystallogr. 1969; 2: 65 71
537 47. Rinaldi R, Sacerdoti M, Passaglia E. Stratlingite: Crustal structure, chemistry and a
538   re-examination of its polytype vertuminite. Eur J Mineral 1990; 2: 841-849
539 48. Ruan CD, Ward CR. Quantitative X-ray powder diffraction analysis of clay
540   minerals in Australian coals using Rietveld methods. Appl Clay Sci. 2002; 21: 227
541   240.
542 49. Sabir BB, Wild S, Bai J. Metakaolin and calcined clays as pozzolans for concrete: a
543   review. Cem Concr Comp 2001; 23: 441-454
544 50. Santacruz I, García de la Torre A, Álvarez-Pinazo G, Cabeza A, Cuesta A, Sanz J,
545   García Aranda MA. Structure of stratlingite and effect of hydration methodology on
546   microstructure. Adv Cem Res. 2016; 28: 13-22.
547 51. Santos A, Gameiro A, Grilo J, Veiga R, Velosa A. Long term behaviour of lime-
548   MK pastes at ambient temperature and humid curing condition. Appl Clay Sci.
549   2014; 88-89:49-55.
550 52. Serry MA, Taha AS, El-Hemaly SAS, El-Didamony H. Metakaolin-lime hydration
551   products. Termochimica Acta 1984; 79:103-110.
552 53. Siddique R, Klaus J. Influence of MK on the properties of mortar and concrete: A
553   review. Appl Clay Sci. 2009; 43:392-400 (2009).
554 54. Taylor HFW. Cement Chemistry, 2nd edition, Thomas Telford Services Ltd,
555   London; 1997.
556 55. Zibouche F, Kerdjoudi H, d Éspinose JB, Damme HV. Geopolymers from Algerian
557   metakaolin. Influence of secondary minerals. Appl Clay Sci.2009; 43: 453-458
558
559
560
561
562
563
564
565
566
567
568
569
570
571
572
573
574
575
576
577

578
579
580
581
582
583
584
585
586
587
588
589
590
591
592
593
594
595
596
597   Figure captions
598
599   Figure 1. Device used for 15 year curing
600
601   Figure 2. XRD spectrum for 15 year paste
602
603   Figure 3. SEM images: a) aluminate crystals and b) strätlingite crystals
604
605   Figure 4. SEM images: a) fibres; b) and c) feldspar forming on conglomerate; d) calcite
606   crystals
607
608   Figure 5. Calcium zeolites forming on conglomerate (a and b)
609
610   Figure 6. Micro-Raman spectrum of the sample (laser $\lambda = 785$ nm); C = calcite; Z =
611   zeolite.
612
613   Figure 7. NMR spectrum for the 15 year MK/lime sample: a) ^{27}Al MAS and b) ^{29}Si
614   MAS NMR.
615
616   Figure 8. FT-IR spectrum for the 15 year paste
617
618   Figure 9. TG/DTA thermogram for the 15 year paste
619
620   Figure 10. Gismondine formation by cycling of C-H-S double chains
621
622
623
624
625
626
627

628
629

Table 1. Chemical composition of raw MK (%)

Oxide	SiO_2	Al_2O_3	Fe_2O_3	CaO	MgO	SO_3	Na_2O	K_2O	TiO_2	LOI
MK	51.60	41.60	4.64	0.09	0.16	-	0.01	0.62	0.83	0.60

Oxide (%)	C_4AH_{13}	C_2ASH_8	Conglomerates	Fibre	Gismondine	Garronite	Feldspar
Na_2O	n.d.	1.43±0.39	3.49±0.55	5.28±0.82	1.32±0.56	1.87±0.69	1.53±0.79
MgO	n.d.	n.d.	0.64±0.08	n.d.	n.d.	n.d.	n.d.
Al_2O_3	22.92±0.82	25.12±2.27	29.34±1.79	11.72±0.94	38.00±1.96	33.10±2.51	33.29±2.35
SiO_2	1.43±0.12	13.66±1.58	51.24±0.87	17.44±0.65	40.94±2.18	47.3±2.36	47.75±1.28
K_2O	n.d.	1.46±0.72	1.99±0.38	n.d.	n.d.	n.d.	0.75±0.12
CaO	75.65±1.27	58.33±1.27	13.30±0.72	65.56±0.41	19.74±1.64	17.66±1.29	16.68±0.69
Si/(Si+Al)	-	-	-	-	0.51	0.58	-

Table 2. SEM/EDX analysis of the 15 years paste

n.d. = not detected

Figure 1
Click here to download high resolution image

60ºC

lid

water

sand
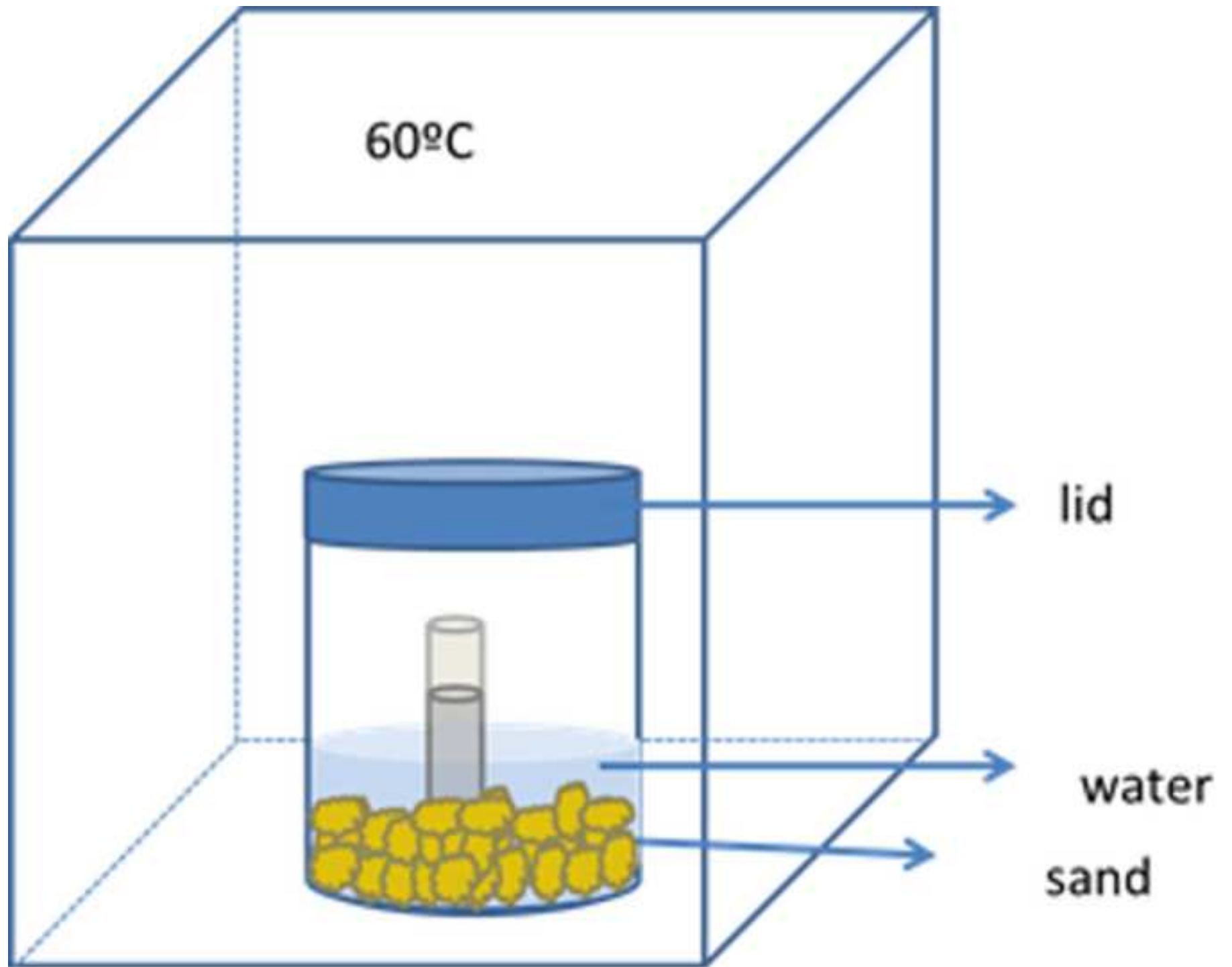
Figure 2
Click here to download high resolution image
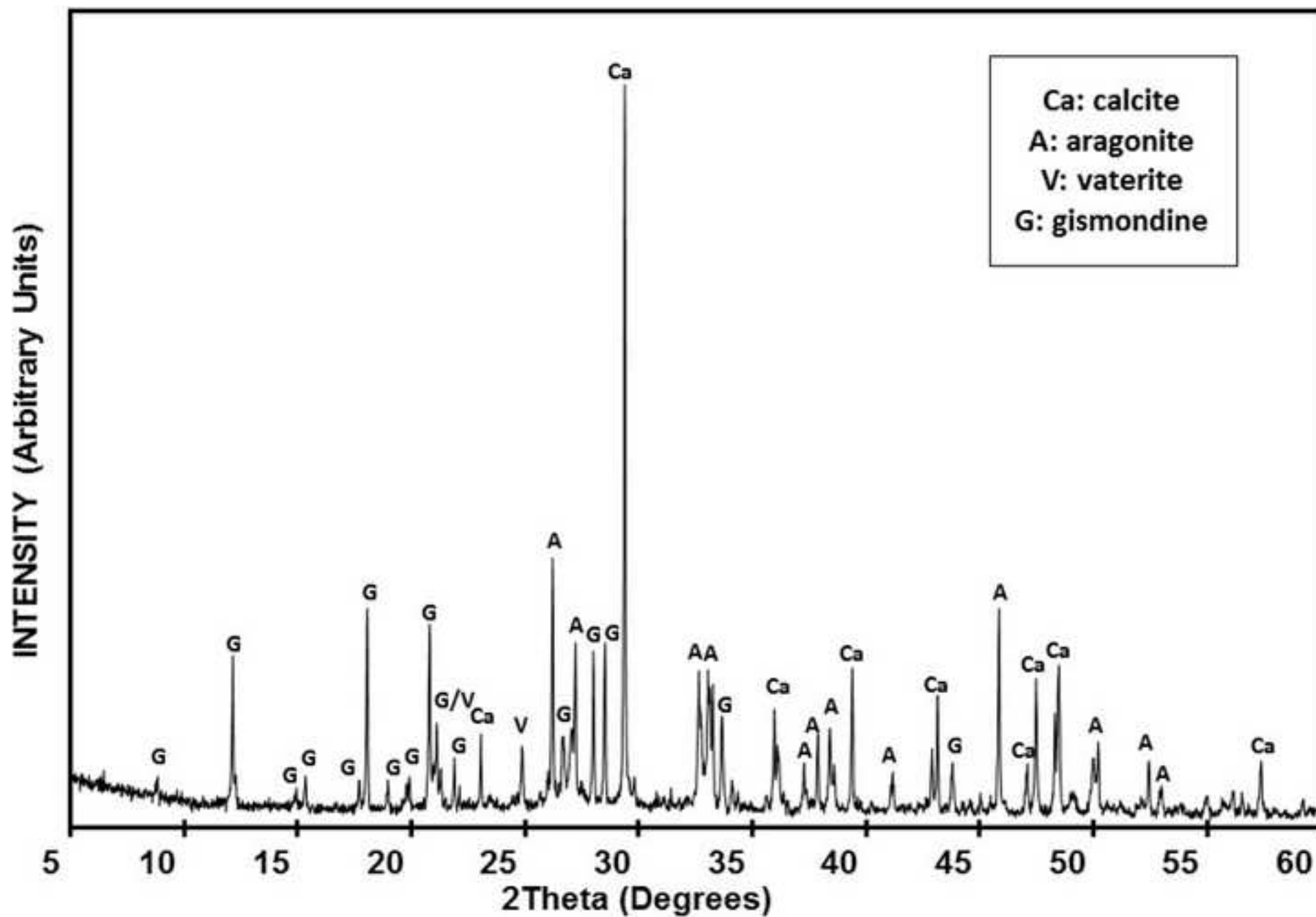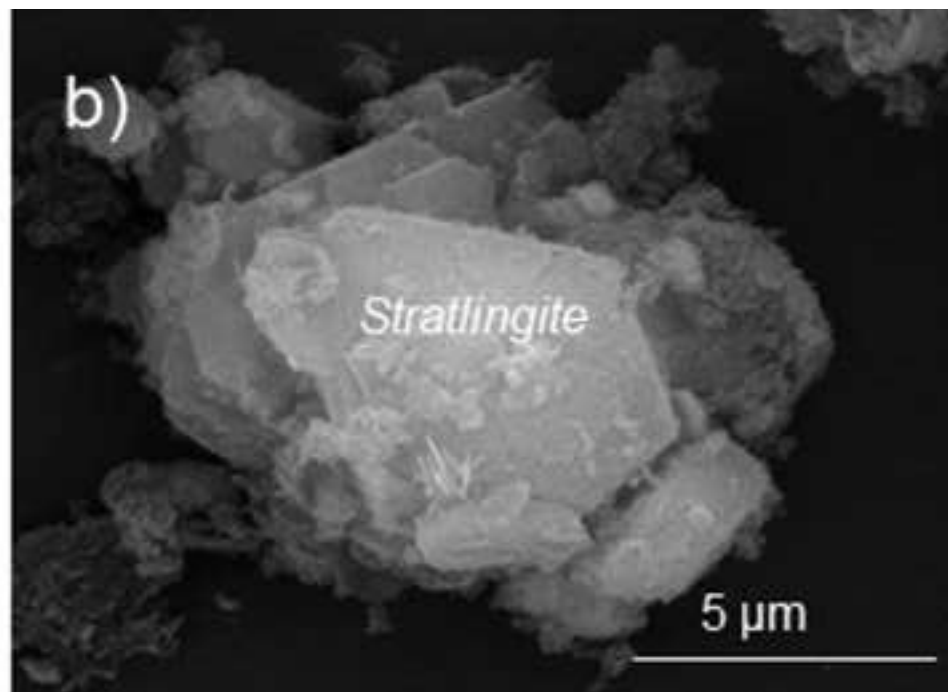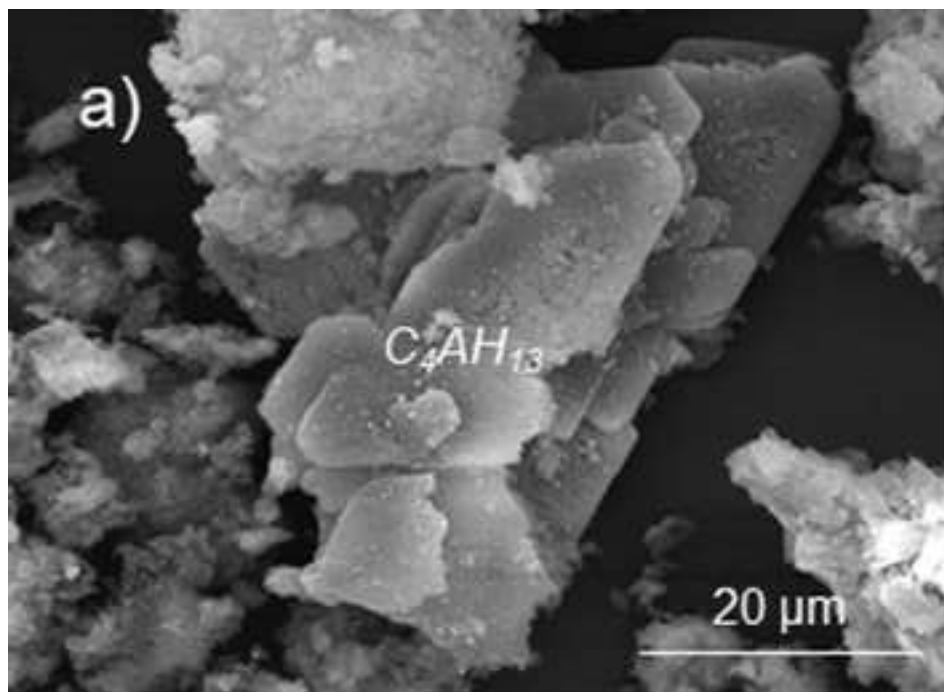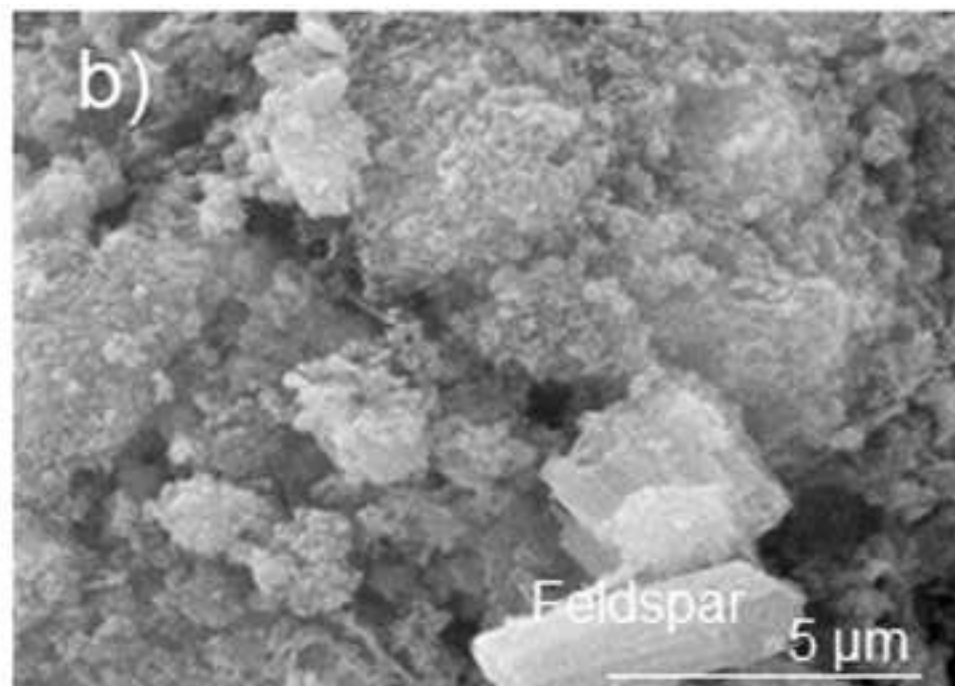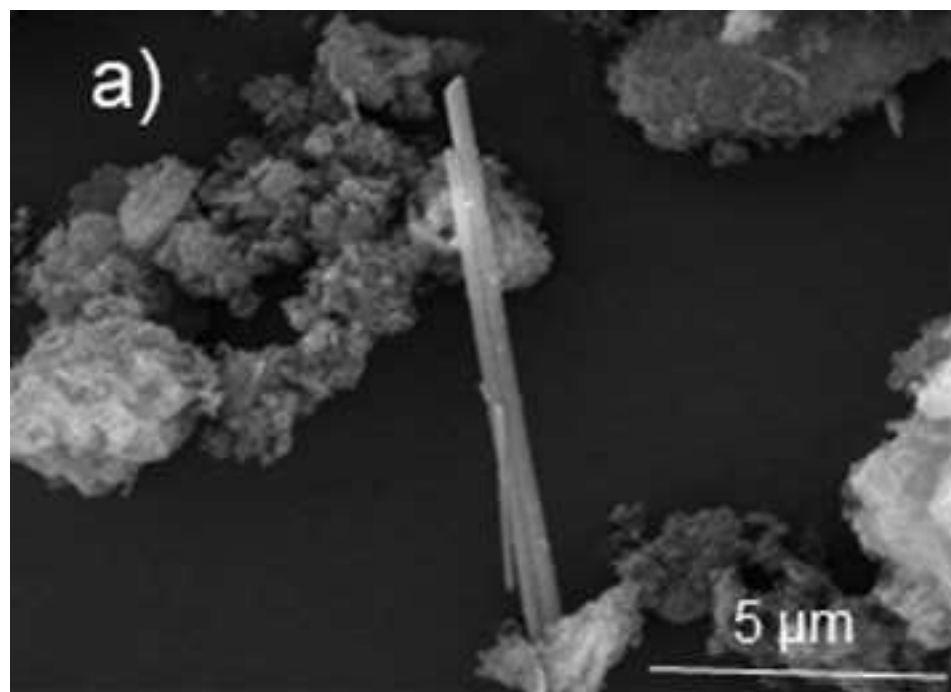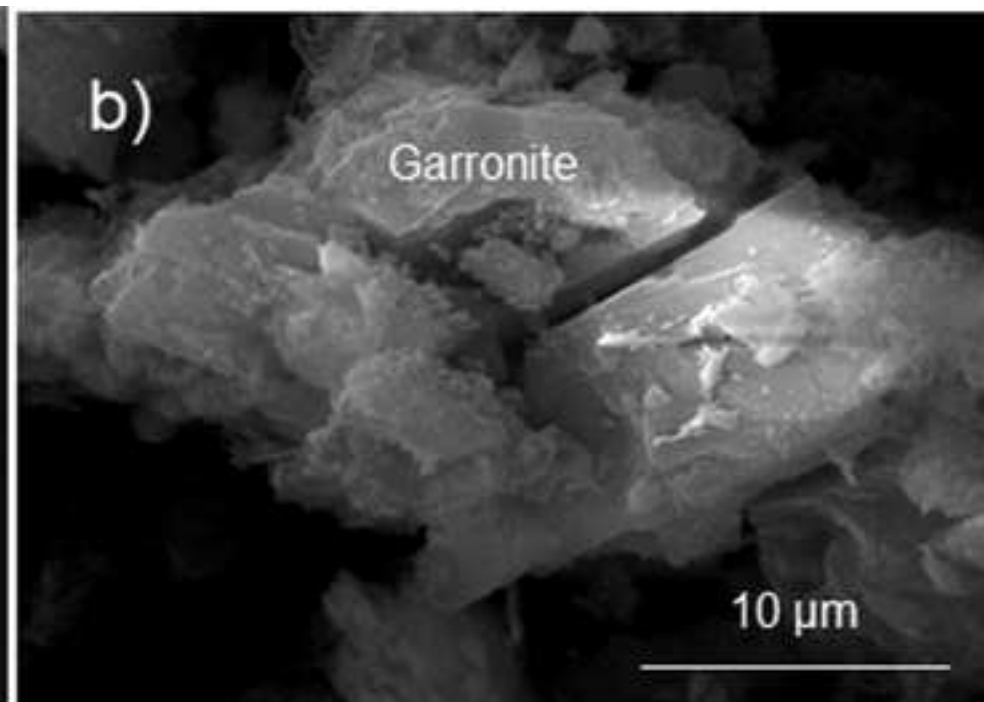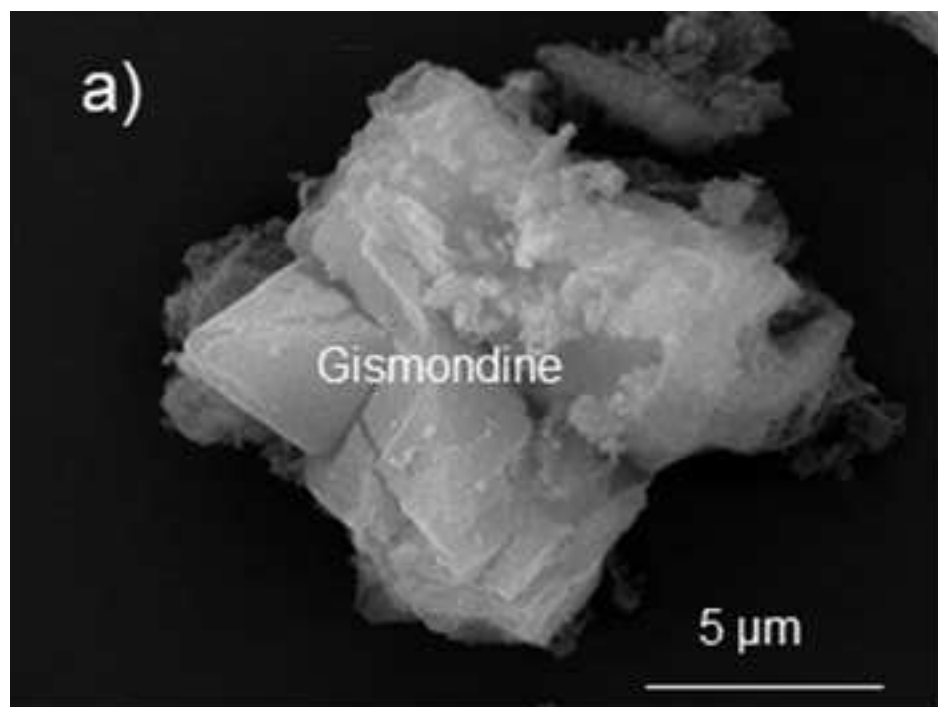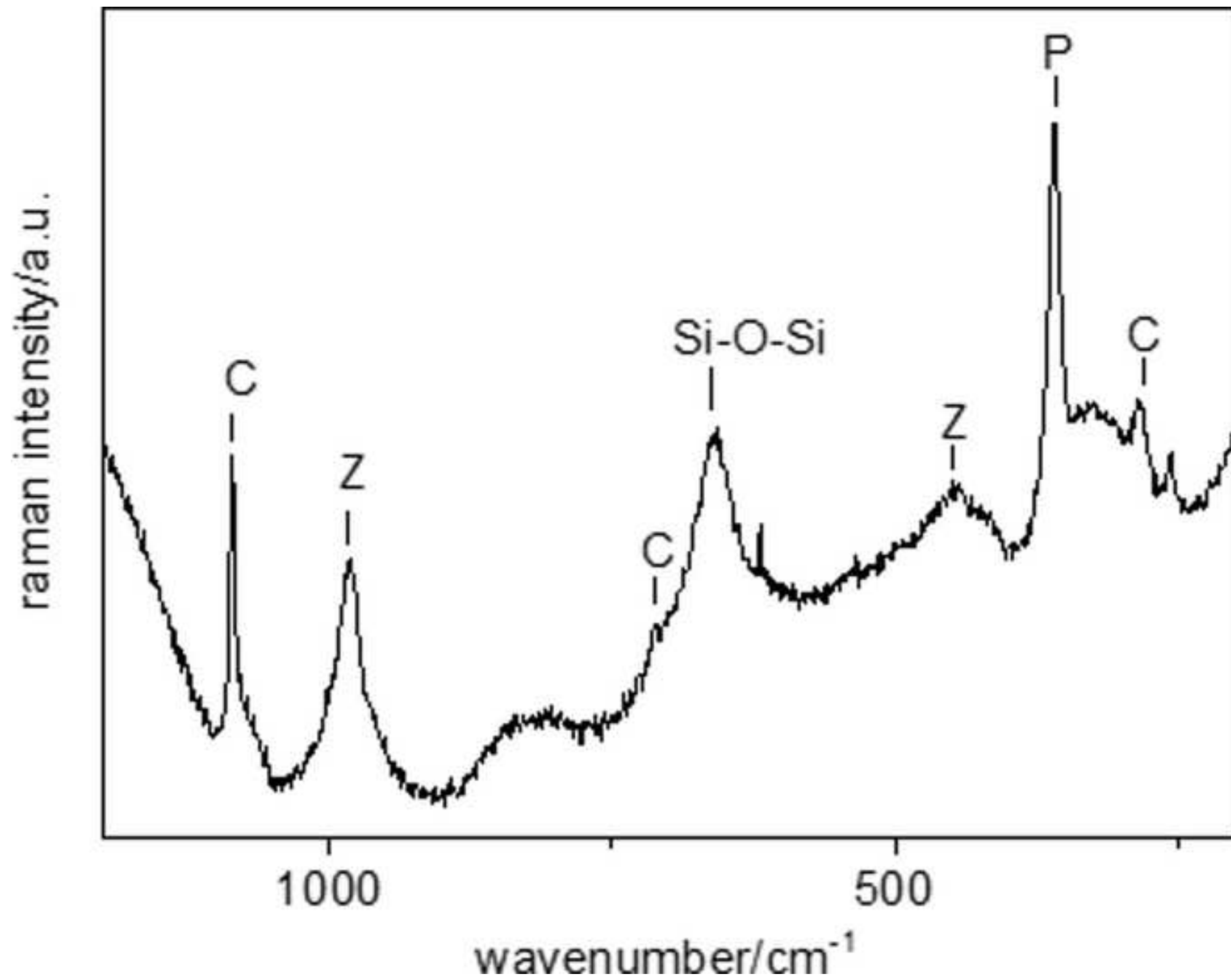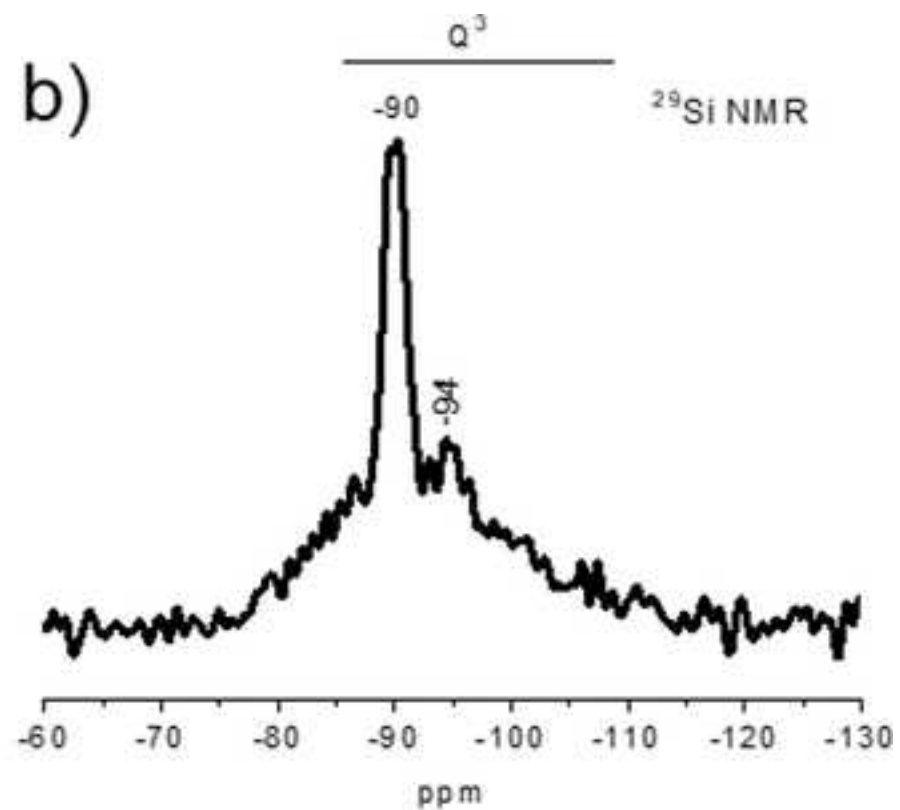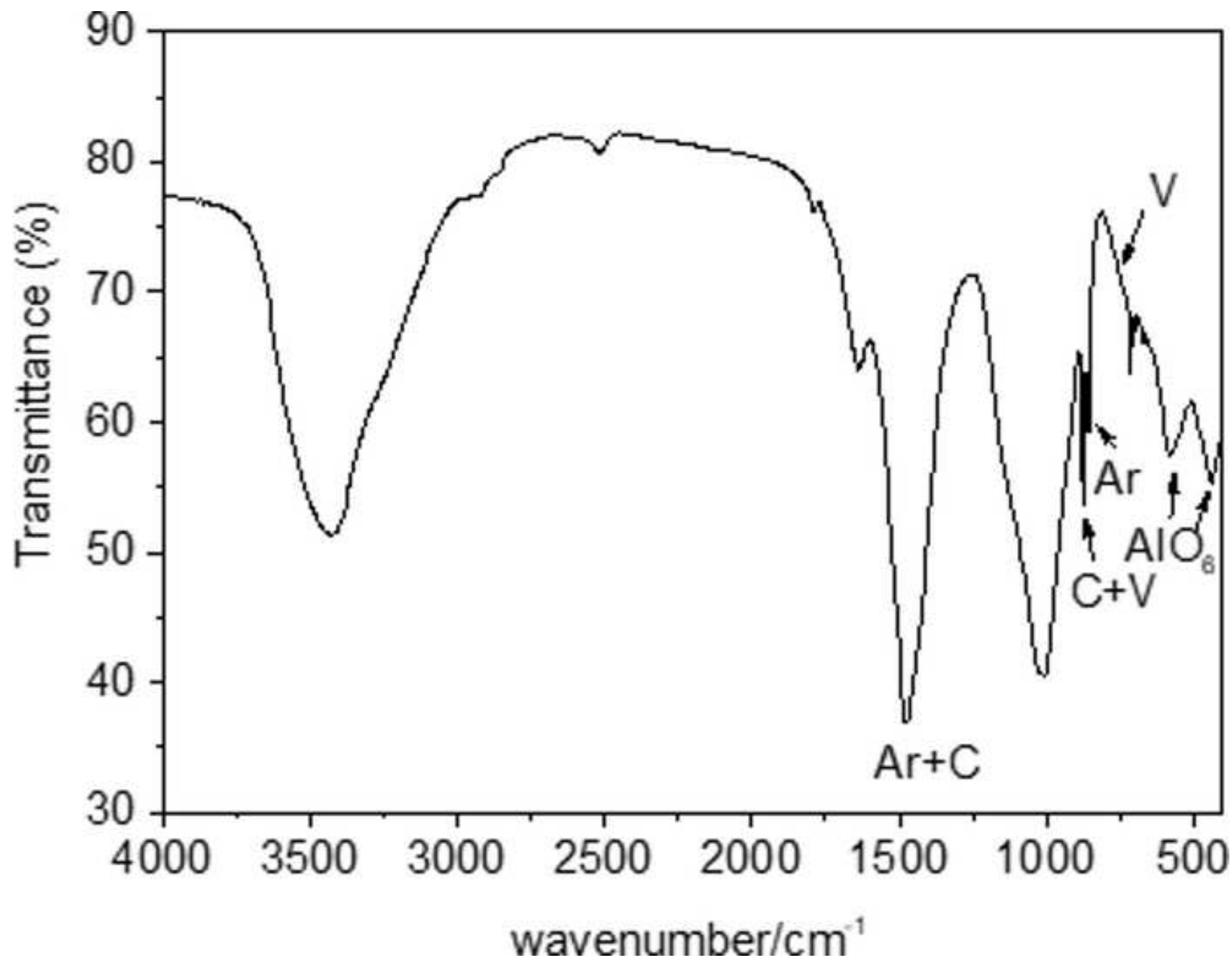
Figure 4
Click here to download high resolution image

a) 5 μm

b) Feldspar 5 μm

c) Feldspar Carbonates 5 μ m

d) Carbonates 5 μm
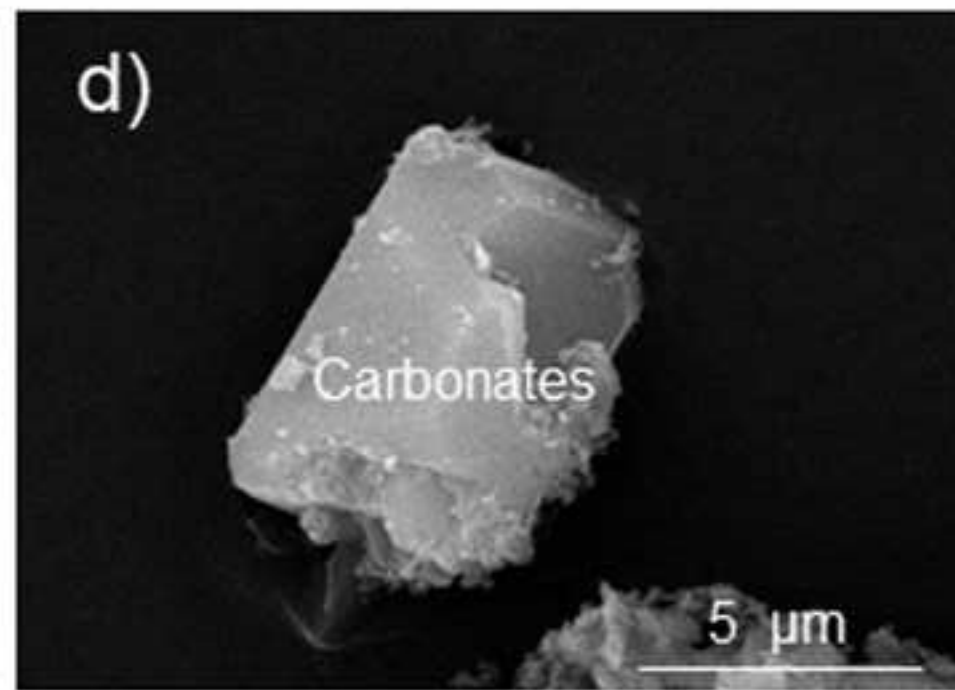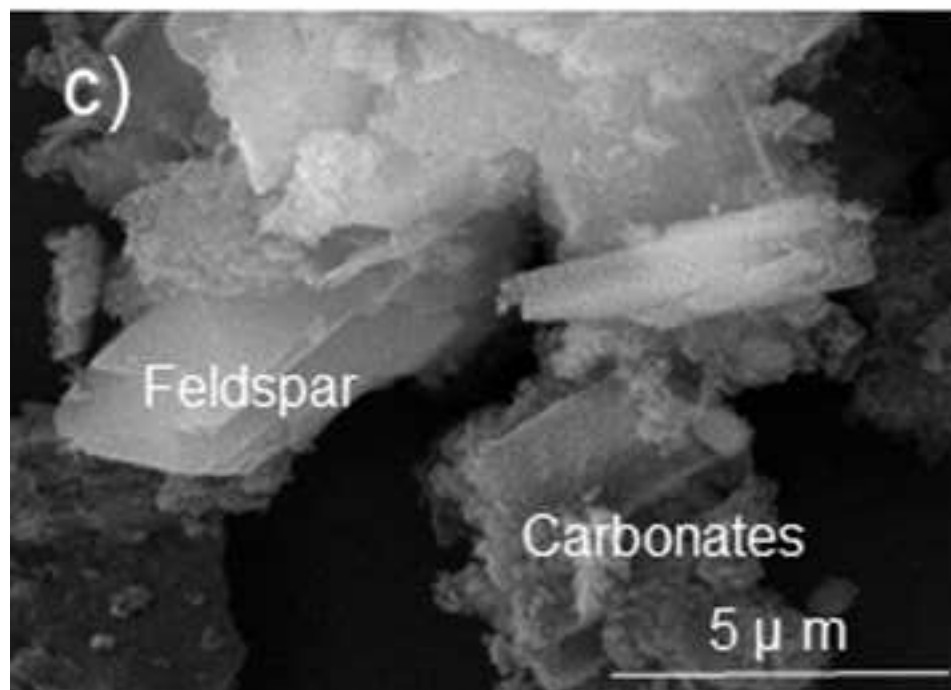
Figure 6
Click here to download high resolution image
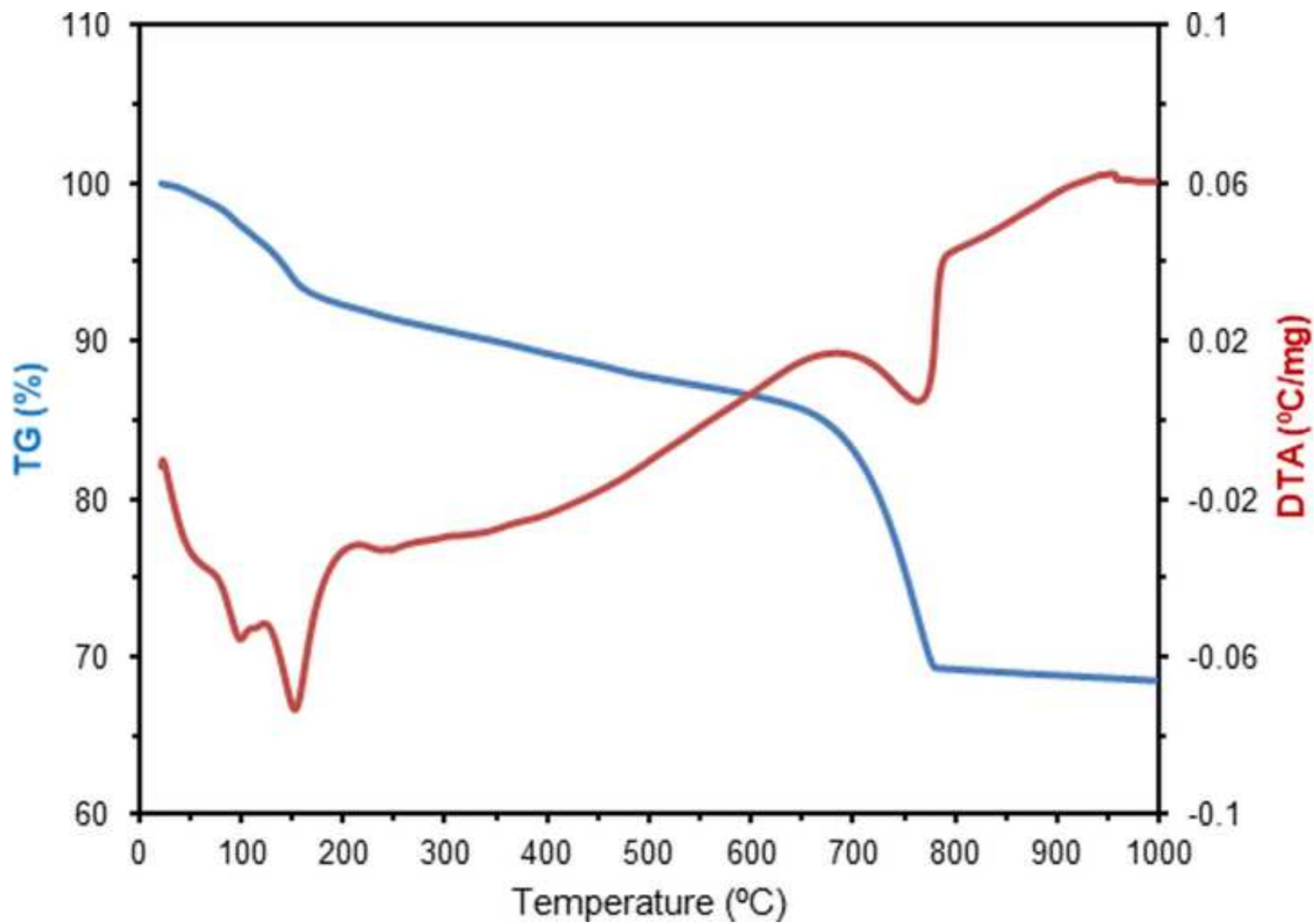
Figure 7
Click here to download high resolution image
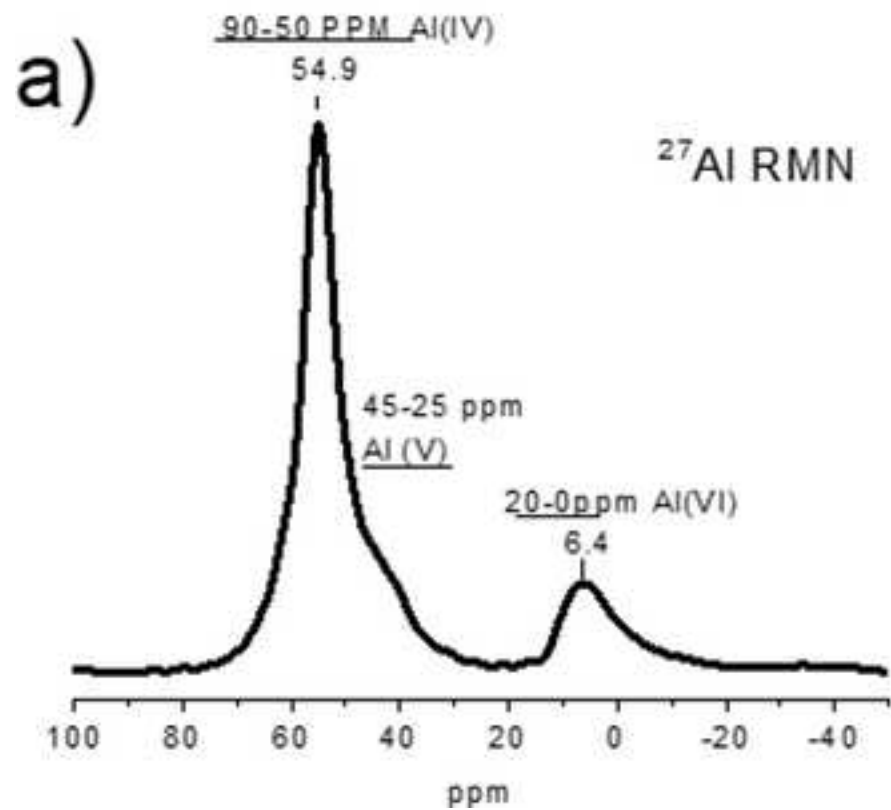
Figure 8

Figure 10
[Click here to download high resolution image](#)